Anion Redox in an Amorphous Titanium Polysulfide

Keiji Shimoda,*,† Kentaro Kuratani,‡ Shunsuke Kobayashi,§ Tomonari Takeuchi,‡ Miwa Murakami,† Akihide Kuwabara,§ Hikari Sakaebe‡

† Office of Society-Academia Collaboration for Innovation, Kyoto University, Uji, Kyoto 611-0011, Japan

‡ National Institute of Advanced Industrial Science and Technology, Ikeda, Osaka 563-8577, Japan

§ Nanostructures Research Laboratory, Japan Fine Ceramics Center, Atsuta, Nagoya 456-8587, Japan

ABSTRACT

Amorphous transition metal polysulfides are promising positive electrode materials for next-generation rechargeable lithium-ion batteries because of their high theoretical capacities. In this study, sulfur anion redox during lithiation of amorphous TiS_4 (a-TiS_4) was investigated using experimental and theoretical methods. It was found that a-TiS_4 has a variety of sulfur valence states such as S^{2-}, S^-, and $S^{\delta-}$. The S^{2-} species became the main component in the Li_4TiS_4 composition, indicating that sulfur is a redox-active element up to this composition. The simulated a-TiS_4 structure changed gradually by lithium accommodation to form a-Li_4TiS_4: S-S bonds in the disulfide units and polysulfide chains were broken. Bader charge analysis suggested that the average S valency decreased drastically. Moreover, deep lithiation of a-TiS_4 provided a conversion reaction to metallic Ti and Li_2S, with a high practical capacity of ~1000 mAh g^{-1} when a lower cut-off voltage was applied.

1

KEYWORDS

Lithium-sulfur batteries; Amorphous transition metal polysulfides; Anion redox; Operando NMR spectroscopy; X-ray photoelectron spectroscopy; Density functional calculations

*Corresponding author:

Keiji Shimoda

Office of Society-Academia Collaboration for Innovation, Kyoto University, Gokasho, Uji 611-0011, Japan

ORCID iD: orcid.org/0000-0003-4600-3437

E-mail address: shimoda.keiji.6v@kyoto-u.ac.jp

Tel: +81-774-38-4967

Fax: +81-774-38-4996

1. INTRODUCTION

Elemental sulfur (S) is among the most promising electrode materials for next-generation rechargeable lithium-ion batteries (LIBs) because of its high theoretical capacity ($S + 2Li^+ + 2e^-$ $\rightleftarrows$ Li_2S; 1672 mAh g^{-1}). This involves the S^0/S^{2-} redox couple at an average potential of 2.15 V vs. Li/Li$^+$.[1] However, S and Li_2S are electrically resistive, and the dissolution of lithium polysulfide intermediates Li_2S_x ($2 < x < 8$) in nonaqueous electrolyte solutions has been reported during the discharge–charge cycles.[1-3]

Nanostructured carbon-sulfur composite electrodes were developed to compensate for the low electric conductivities of S and Li_2S.[4-6] Conductive carbon housings were designed to effectively confine and suppress the dissolution of S. As an alternative approach, sulfur-rich transition metal (TM) sulfides (MS_x, $x > 3$) have been considered as new electrode materials for "advanced" Li-S batteries, which were designed to improve conductivity and suppress polysulfide dissolution by introducing strong M-S bonds. Amorphous molybdenum polysulfides (a-$MoS_{3.4}$ and a-$MoS_{5.7}$) were synthesized from crystalline precursor materials, where the S/M ratio depends on the composition of the precursor.[7, 8] The sulfur-rich TM sulfides are often prepared by mechanochemical alloying of the metallic powder or its sulfides with S or Li_2S because it is a simple technique to control the S/M ratio in materials.[9-14] In most cases, these sulfides become amorphous. Amorphous host structure can allow high S/M ratios. Several amorphous niobium polysulfides (a-NbS_x, x = 3, 4, and 5) were prepared.[11] Their initial discharge capacities were reported to be 281, 446, and 596 mAh g^{-1}, respectively, showing improvement with increasing amounts of sulfur in the material. An Fe-substituted Li_2S-based material, Li_8FeS_5 ($[Li_{0.8}Fe_{0.1}\bullet_{0.1}]_2S$, where $\bullet$ means vacancy), showed a high discharge capacity of ~730 mAh g^{-1}.[15] The low-crystalline antifluorite structure of pristine Li_8FeS_5 changed to amorphous by Li extraction. Sulfur

3

anion redox during Li extraction from Li_8FeS_5 was confirmed by S K-edge X-ray absorption spectroscopy (XAS) and X-ray photoelectron spectroscopy (XPS) techniques.[15, 16]

Among the sulfur-rich TM sulfides, vanadium tetrasulfide (VS_4) has a crystalline form. The crystalline VS_4 (c-VS_4) shows Peierls distortion chains of V-V bonds along the c axis, and the V^{4+} ions are coordinated by the disulfide anions $[S_2]^{2-}$.[17, 18] The second discharge capacity of c-VS_4 was reported to be 1066 mAh g^{-1}, in a voltage window between 0.01 and 3.0 V, while the initial capacity was larger than the theoretical capacity due to electrolyte decomposition.[19] X-ray pair distribution function (PDF) analysis and solid-state nuclear magnetic resonance (NMR) spectroscopy were applied to understand the structural changes of c-VS_4 by lithiation.[20] The c-VS_4 chain structure was broken and the conversion to elemental V and Li_2S was reported. Amorphous VS_4 (a-VS_4) was prepared by ball-milling c-VS_4.[21] Its electrochemical properties moderately improved in a voltage window between 1.5 and 3.0 V. The a-VS_4 structure consisted of Peierls-distortion chains similar to that of c-VS_4, and the chain structure changed to $[VS_4]^{3-}$ tetrahedral monomer units by Li insertion.[22] The conversion reaction did not occur within this voltage window.

Amorphous titanium polysulfides, a-TiS_3 and a-TiS_4, were first synthesized by the mechanochemical alloying of TiS_2 and S.[9] The use of TiS_x as an electrode material is expected to be advantageous to the other polysulfides because titanium is a lighter TM element when the S/M ratio is fixed. The a-TiS_4 electrode showed an initial discharging capacity of ~690 mAh g^{-1} in a voltage window between 1.5 and 3.0 V, where ~4 Li ions were expected to be incorporated (Li_4TiS_4; theoretical capacity of 609 mAh g^{-1}). Gradual changes in the amorphous host structure of a-TiS_4 were investigated using PDF, XAS, and density functional theory-based molecular dynamics (DFT-MD) simulation.[23] The S-S disulfide bonds were broken, and the Ti coordination number decreased by Li insertion. Furthermore, the DFT-MD simulated a-TiS_4 and a-Li_4TiS_4 structures suggested a change in the -Ti-S- network connectivity. However, the exact information

4

on the redox mechanism of a-TiS$_4$ during Li insertion is still unclear. Recently, TM polysulfides have received much attention as a good example of anion redox, and were compared to the oxygen anion redox mechanism expected for the Li-rich layered oxides Li[Li$_{1-x}$M$_x$]O$_2$.[24-26] The reversibility of anion redox process should be a key factor for stable high-capacity batteries. The sulfur anion redox in sulfides is expected to be stable compared to the oxygen anion redox in Li-rich oxides, where the latter may involve gas release following irreversible structure change. Therefore, it is important to investigate in detail the redox contribution from TM cation and sulfur anion species in the amorphous TM polysulfides. It is also interesting to discuss a relationship between the anion redox and structural modification in amorphous electrode materials during discharge–charge cycle. Herein, we investigate the structural diversity of an amorphous TiS$_4$ and its changes along with its concomitant sulfur redox mechanism during the lithiation process using experimental and theoretical methods.

2. EXPERIMENTAL AND COMPUTATIONAL METHODS

Amorphous TiS$_4$ was mechanochemically synthesized from a mixture of TiS$_2$ (99.8%, Wako) and S (99.9%, Wako) in a 1:2 molar ratio, for 13 h at 510 rpm in a planetary ball mill (Pulverisette 7, Fritsch).[9, 10] The working electrode comprised a mixture of the active material (a-TiS$_4$), ketjen black (KB), and styrene-ethylene/butylene-styrene (SEBS)-based binder in a 79:8:13 weight ratio on a Ni mesh current collector. A Li foil (>99.9%, Honjo Metal) was used as the negative electrode, and a microporous polyolefin sheet was chosen as the separator. A solution of 1 M LiPF$_6$ dissolved in a 3:7 volume ratio mixture of ethylene carbonate (EC) and ethyl methyl carbonate (EMC) was used as the electrolyte solution (battery grade, Kishida Chemical). The laminate-type cells were assembled in an Ar-filled glove box. Electrochemical measurements during the operando NMR data acquisition were carried out at 30 °C. The cells were cycled between 1.75 and 3.0 V at a

constant current density of 24.3 mA g^{-1} (0.02 C rate, where 1 C = 1217 mA g^{-1}). They were disassembled at selected discharge/charge states in a glove box and rinsed with dimethyl carbonate (DMC) to remove the residual electrolyte solution.

X-ray diffraction (XRD) measurements were performed for the a-TiS$_4$ powder using a D8 ADVANCE diffractometer (Bruker) with a Cu K$_\alpha$ source. Energy-dispersive X-ray spectroscopy (EDS) measurements equipped on a scanning electron microscope (SEM; JSM-6700F, JEOL) were performed to estimate the S/Ti ratio of the synthesized a-TiS$_4$ powder.

Atomic-resolution characterization was performed for the pristine a-TiS$_4$ powder using a spherical aberration-corrected scanning transmission electron microscope (JEM-2400FCS, JEOL) at an accelerating voltage of 200 kV. The probe-forming aperture semi-angle was 22 mrad. High-angle annular dark-field (HAADF) and bright-field (BF) scanning transmission electron microscopy (STEM) images were recorded with a 45–180 mrad and a 0–12 mrad detector, respectively. The composition analysis of the pristine a-TiS$_4$ powder was carried out by an electron energy loss spectrometer (GIF Continuum ER, Gatan) attached to the above scanning transmission electron microscope. The convergence and collection semi-angles were 33 and 43 mrad, respectively. The electron energy loss spectroscopy (EELS) analysis was performed using the Gatan Microscopy Suite software (GMS3.4). For the STEM observations and the EELS analysis, the powder sample was dispersed on holey carbon films supported by a Cu grid in an Ar-filled glovebox. Then, the sample was transferred from the glovebox to the electron microscope using a TEM holder (Mel-Build) without exposure to air.

NMR spectra were collected on a DD2 600 spectrometer (Agilent Technologies) at a magnetic field of 14.1 T. Operando ^{7}Li NMR measurements were carried out using a homemade wide-bore static probe, in which a flat laminate-type cell was placed parallel to the magnetic field in the center

of a 10 mm-diameter solenoid coil.[27] A Hahn echo pulse sequence was used, with a first pulse width of 6 μs and an echo decay of 8 μs. Each spectrum was averaged over 30 min (scan number of 1800 with a relaxation delay of 1 s). The ^{7}Li magic-angle spinning (MAS) NMR measurements were performed using a wide-bore T3 MAS probe (Agilent Technologies). Powdered samples were packed into 1.2 mm ϕ MAS ZrO_2 rotors with airtight caps in an Ar-filled glove box and spun at a rate of 60 kHz during the measurements. A rotor-synchronized Hahn echo pulse sequence (π/2-τ-π-τ-acq.) was used with a π/2 pulse width of 0.8 μs and a relaxation delay of 5 s. All spectra were referenced to 1 M LiCl solution at 0.0 ppm.

XPS measurements were conducted using a PHI5000 VersaProbe II (ULVAC-PHI) photoelectron spectrometer with monochromatic Al K$_\alpha$ radiation (1486.6 eV). The electrode samples were transferred to an ultra-high vacuum sample chamber ($< 4 \times 10^{-7}$ Pa) without exposing them to air. The experimental condition was described elsewhere.[22] Peak fitting procedures were performed using MultiPak (ULVAC-PHI) after Shirley-type background subtraction and energy calibration with respect to the C 1s signal from KB at 284.6 eV.

DFT-MD simulations were carried out for a-Li$_x$TiS$_4$ ($x = 0$, 2, and 4) to visualize the amorphous structures and extract valence and bonding information on each element using CASTEP.[28] The simulation cells for a-TiS$_4$, a-Li$_2$TiS$_4$, and a-Li$_4$TiS$_4$ contained 80, 112, and 144 atoms, respectively. MD simulations were performed using ultrasoft pseudopotentials with a plane-wave cut-off energy of 310 eV and moderate convergence tolerances to accelerate the time-consuming structure annealing process. The cells were initially annealed at 5000 K for 5000 MD steps (1.0 fs/step) in the NVT ensemble (N: number of particles, V: volume, T: temperature). They were subsequently annealed at 4000, 3000, 2000, and 1000 K for every 2500 steps. The cells were annealed at 1000 K for another 2500 steps in the NPT ensemble (P: pressure) and then at 300 K for 5000 steps.

Finally, the atomic positions and cell parameters were fully relaxed until the residual forces and stresses acting on each atom were less than 0.01 eV/Å and 0.02 GPa, respectively. GGA-PBEsol was employed for the exchange-correlation functional.[29] The *k*-point sampling for the Brillouin zone integration was conducted according to the Monkhorst-Pack scheme with a grid spacing of 0.07 Å^{-1}. Norm-conserving pseudopotentials with a cut-off energy of 770 eV and the hybrid functional HSE06 were employed for the electronic density-of-states (DOS) calculations.[30] Ultrasoft pseudopotentials generated on-the-fly were employed with a cut-off energy of 600 eV and a grid spacing of 0.04 Å^{-1} for the NMR parameter calculations, where the magnetic shielding tensors (σ) were calculated using the gauge-including projector-augmented wave (GIPAW) approach.[31, 32] The simulated structures were visualized using the VESTA software.[33]

3. RESULTS AND DISCUSSION

Figure 1 shows the XRD profile of a-TiS$_4$ powder prepared by ball milling, showing no reflections of the starting materials. The XRD profiles of the ball-milled TiS$_2$ and S samples were also shown in Figure S1. The ball-milled S remained in crystalline form, indicating that all the sulfur reacted with TiS$_2$ during the preparation of a-TiS$_4$. The XRD profile of the pristine a-TiS$_4$ showed broad halo patterns characteristic of amorphous material, whereas the diffraction peaks of a nanocrystalline component seemed overlapping.

To further characterize the as-prepared a-TiS$_4$, the HAADF/BF STEM images and EELS map were acquired (Figure 2). The EELS composition maps indicated the uniform distribution of Ti and S in the scale of several tens nm, and the S/Ti ratio was estimated to be 3.8 (S/Ti = 79.2 at.%/ 20.8 at.%). The bulk S/Ti ratio was also determined to be 3.8 by SEM-EDS, and these values were close to the nominal composition within the analytical precision (< ±5%). A small titanium-rich

grain indicated by a white arrow in Figure 2 was also observed, where the S/Ti ratio was ~2.4 (S/Ti = 70.3 at.%/ 29.7 at.%). The electron diffraction (ED) profile of the pristine a-TiS$_4$ resembled the XRD profile (Figure S2). The simulation profile suggested the formation of nanocrystalline TiS$_3$. The lattice contrasts attributed to TiS$_3$ were observed in the high magnification HAADF/BF images (Figures S3 and S4). Based on the estimation of volume fraction from the BF image, the pristine a-TiS$_4$ prepared in this study may consist of the amorphous phase of the TiS$_4$ composition by 86% and the nanocrystalline TiS$_3$ by 14% (Figure S5). Longer milling time and/or higher rotating condition during the milling process will provide a homogeneous amorphous material.[10] Figure S6 shows Raman spectra of the pristine a-TiS$_4$ sample, where the lattice vibrations of TiS$_3$ were observed.[34] After the first cycle, the nanocrystalline TiS$_3$ has disappeared, and an amorphous material was formed. We therefore believe that the presence of a small amount of TiS$_3$ in the pristine electrode does not affect the following discussion.

To understand the lithiation/delithiation behavior of a-TiS$_4$, operando ^{7}Li NMR measurements were conducted. A gentle voltage sloping was observed from the discharge–charge profile of a Li//a-TiS$_4$ operando NMR cell with a voltage window between 1.75 and 3.0 V (Figure 3a). The discharge–charge profile in this study resembled that in the previous study[9] but still showed slightly larger polarization, probably due to the faster current rate applied here. The initial discharging and charging capacities were 636 and 574 mAh g^{-1}, respectively. The discharging capacity corresponds to a composition similar to that of Li$_4$TiS$_4$, assuming that contributions from the side reactions, such as electrolyte decomposition, are small. Figure 3b shows the operando ^{7}Li NMR spectra during the discharging (lithiation) process, where the initial spectrum before the electrochemical test was subtracted to avoid a large signal from the LiPF$_6$ salt in the electrolyte solution at ~0 ppm. A relatively broad signal appeared during lithiation at ~2.5 ppm, which linearly increased in intensity and shifted very slightly to higher frequencies. This signal is attributed to the Li ions

inserted in a-TiS$_4$ (i.e., a-Li$_x$TiS$_4$). Considering the peak position and width of the signal, the tentative a-Li$_x$TiS$_4$ ($x \leq 4$) is a diamagnetic Ti^{4+}-containing material up to the Li$_4$TiS$_4$ composition, suggesting that Ti ions remain tetravalent. The spectral evolution was reversible (Figure 3c). The integrated intensity of the a-Li$_x$TiS$_4$ signal almost linearly increased and decreased (Figure S7). Moreover, complicated signal contributions from the reductive and oxidative decomposition of the electrolyte solution were visible at ~0 ppm. The signal from the decomposition product could not be fully subtracted using the initial spectrum before the electrochemical test. Figure 3d shows the high-resolution ^{7}Li MAS NMR spectra for the disassembled samples. The spectra were normalized by the scan number and sample weight in the rotors. A sharp peak was observed at 1.7 and 2.4 ppm for the half-discharged (#2) and full-discharged (#3) samples, respectively, further indicating the diamagnetic nature of the a-Li$_x$TiS$_4$ signals. Furthermore, the peak shifts observed in operando and MAS NMR spectra suggest that a-Li$_x$TiS$_4$ ($x \leq 4$) is not a two-phase mixture of a-TiS$_4$ and a-Li$_4$TiS$_4$, and the a-Li$_x$TiS$_4$ structure changes continuously during Li insertion. After delithiation (#4), a small signal originating from the decomposition product was observed at 0 ppm.

XPS is a suitable technique to quantitatively characterize the chemical species of sulfur in sulfide materials, although this technique includes near-surface valence information. The Ti 2p and S 2p XPS spectra of the a-TiS$_4$ electrode samples are compared in Figure 4. The Ti 2p core-level spectra split into two components, p$_{3/2}$ (454–460 eV) and p$_{1/2}$ (460–466 eV) with an intensity ratio of 2:1, owing to spin-orbit coupling (Figure 4a). These components were best fitted using pseudo-Voigt functions by introducing asymmetry parameters. The Ti 2p$_{3/2}$ peak position of the pristine a-TiS$_4$ (456.3 eV) is close to that of TiS$_2$ (455.9, 456.1 eV[35]) and TiS$_3$ (455.9, 456.0 eV[35, 36]), which is attributed to the Ti^{4+} valence state in sulfides. The peak positions of the a-TiS$_4$ electrode samples were within the range of 456.0–456.3 eV, indicating that the tetravalent state was maintained

during lithiation. An additional component, centered at 458–459 eV, was attributed to the satellite feature of the main peak. During the lithiation, a shoulder peak seems appear at ~458 eV, which may include a minor contribution from titanium oxides. The S 2p core-level spectra can be described by three sets of doublet peaks of $p_{3/2}$ and $p_{1/2}$ with an intensity ratio of 2:1 formed due to spin-orbit coupling (Figure 4b). These peaks were best fitted using pseudo-Voigt functions that were 90% Gaussian and 10% Lorentzian. A peak separation of 1.18 eV and a common peak width were applied for each $p_{3/2}$ and $p_{1/2}$ pair. Pristine a-TiS$_4$ (#1) showed three $p_{3/2}$ peak components at 161.3, 162.5, and 163.4 eV. The first one was believed to originate from the S^{2-} species with a chemical shift of slightly higher binding energy than that of TiS$_2$ (160.5, 160.9 eV[35]) but similar to that of TiS$_3$ (S^{2-}; 161.0, 161.2, 161.6 eV[35-37]). The second and third components were assigned to the S^- ($[S_2]^{2-}$ disulfide and/or terminal S in the -S-S-S- polysulfide chain) and $S^{\delta-}$ ($\delta \approx 0$, central S in the -S-S-S- polysulfide chain) species with chemical shifts close to those of TiS$_3$ (S^-; 162.3, 162.4, 162.8 eV[35-37]) and S (163.6, 163.9 eV[38, 39]), respectively. Even though only the S^- species was expected to be present based on the chemical composition, intensity ratio of $S^{2-}:S^-:S^{\delta-}$ in a-TiS$_4$ was estimated to be 22:45:34. Therefore, a-TiS$_4$ exhibits a variety of sulfur chemical species, which is also different from the mixing state of TiS$_2$ and S (Figure S8). The escape depth of the S 2p photoelectrons is approximately 15 monolayers (40–50 Å) from the particle surface when the Al K$_\alpha$ source is used.[36] Here, TiS$_2$ was used to roughly estimate the contribution from the sulfur species at the outermost surface layers. Although the crystalline TiS$_2$ has only S^{2-} species in the bulk, the S 2p spectrum showed the $S^{2-}:S^-$ intensity ratio of 89:11 (not shown). Therefore, the S 2p spectra represent ~90% contribution from the subsurface-to-bulk region (<50 Å in thickness), and the remaining ~10% originates from the outermost surface layers that experience surface reconstruction, making S-S bonds (<5 Å in thickness). This indicates that the changes in relative

intensity ratio of the sulfur species in the XPS spectra can be mostly treated as the changes in the bulk. The chemical shifts of the S^{2-} and S^- species slightly decreased in energy during the lithiation process (Figure 4c), suggesting an increased ionic character in a-Li$_x$TiS$_4$. A similar behavior was reported for the lithiation of a-TiS$_3$.[37] Moreover, the S 2p spectra of the fully discharged sample (#3) showed an increase in S^{2-} at the expense of S^- and $S^{\delta-}$ (S^{2-}:S^-:$S^{\delta-}$ = 53:26:21). This strongly indicates that Li insertion was charge-compensated by sulfur through the breakage of disulfide bonds and polysulfide chains (Figure 4d). The chemical state of sulfur in the charged electrode (#4) almost returned to that of the pristine material.

The a-TiS$_4$, a-Li$_2$TiS$_4$, and a-Li$_4$TiS$_4$ model structures were obtained from the DFT-MD simulations (Figure 5). The number of atoms in the simulations were small due to the limited computational cost of this study, which led to statistically inaccurate results, and therefore, need to be discussed qualitatively. The calculated PDFs ($g(r)$; Figure S9) reproduced the experimental results obtained in a previous study.[23] In the a-TiS$_4$ model structure, the average S-S and Ti-S distances were 2.09 and 2.46 Å, respectively, and the average coordination number of Ti was 6.9 (6-coord.:7-coord. = 13:87, with a cut-off distance of 3.2 Å). All Ti ions were interconnected via bridging S ions of the Ti-S-Ti network. The a-TiS$_4$ structure shows a variety of sulfur environments: bridging S ions, S-S disulfides, and -S-S-S- polysulfides. Long chains of -S-S-S- polysulfides were available (maximal S$_4$ chains in the present simulation cell), but they were bound to Ti ions, which suppress their dissolution into the organic electrolyte solution. A brief summary of structural information for TiS$_2$, TiS$_3$, and a-TiS$_4$ was listed in Table S1. The a-Li$_2$TiS$_4$ structure has the average S-S distance of 2.13 Å. Instead of long polysulfide chains, disulfide bonds were observed in this structure. The average Ti-S distance and coordination number were 2.41 Å and 6.0, respectively. Various Ti coordination environments were obtained (4-coord.:5-coord.:6-

coord.:7-coord.:8-coord. = 6:19:50:19:6). The average Ti-S distance and coordination number for a-Li$_4$TiS$_4$ were 2.35 Å and 4.9 (4-coord.:5-coord.:6-coord. = 38:38:25), respectively. All the S-S disulfide bonds were broken, and non-bridging and isolated S ions (i.e., Ti-S-Li and Li-S-Li) were observed. Therefore, the Ti-S-Ti network was partly broken, as also pointed out in the literature.[23] These results indicate structural changes, such as decrease in the Ti coordination number and breakage of the S-S bonds and Ti-S-Ti network, during lithiation.[23] The DOS spectra of the model structures suggest that all structures were diamagnetic and insulating (Figure S10).

Bader charge analysis is a suitable method to estimate the ionic charge partitioning on each atom of any solid from the calculated electron density.[40, 41] The average Bader charges of the model structures along with some crystalline references are listed in Table 1. The average Bader charges of the Ti and S ions in a-TiS$_4$ (Ti: +1.64, S: –0.41) were different from the expected formal charges (Ti: +4, S: –1), suggesting strong covalent interactions between these ions. The average Bader charges of the Ti ions slightly increased by lithiation, and these values were within those for Ti^{4+}-containing sulfides (TiS$_2$ and TiS$_3$, Table 1). This indicates that Ti valency of +4 is the formal charge in a-TiS$_4$, a-Li$_2$TiS$_4$, and a-Li$_4$TiS$_4$, which is consistent with the experimental results discussed above.

In contrast, the average Bader charges of the S ions were significantly decreased by lithiation (Table 1). This strongly indicates that sulfur is a redox-active element. The simulated structures were found to involve a variety of sulfur chemical environments (Figure 5). Figure 6a shows the Bader charge distribution of S ions in the model structures. Based on this distribution, three S chemical species were identified in a-TiS$_4$. The most oxidized species has an average Bader charge of –0.06, corresponding to the central S ions in the polysulfide chains. The second one has an average Bader charge of –0.40, which is attributable to the disulfide units and terminal S ions in the polysulfide chains. The last one has an average Bader charge of –0.85, which is considered to

denote the bridging S ions of the Ti-S-Ti network. These sulfur chemical states correspond to the $S^{\delta-}$, S^-, and S^{2-} species in the XPS analysis discussed above. The atomic ratio of S^{2-}:S^-:$S^{\delta-}$ for the simulated a-TiS$_4$ structure was 19:59:22, which is qualitatively consistent with the experimental results. In a-Li$_2$TiS$_4$, the $S^{\delta-}$ species almost disappeared because the polysulfide chains were broken (only one S$_4$ chain was observed; Figure 5b). The S^- species in disulfide and the remaining S^{2-} species had average charges of –0.61 and –1.21, respectively. The Bader charge distribution for a-Li$_4$TiS$_4$ showed two average values of –1.36 and –1.94. Both values correspond to the S^{2-} chemical states in different structural environments. The former originates from bridging and non-bridging S ions, while the latter was close to that in Li$_2$S (Table 1), indicating a highly ionic character of the isolated S ions bound only with Li ions. The simulated a-Li$_4$TiS$_4$ structure contained only the S^{2-} species. This is quite different from the XPS results, where a measurable amount of S^- and $S^{\delta-}$ species was obtained. Such a discrepancy may originate due to significant contributions from the outermost surface reconstruction layer in the XPS spectra and the limited cell size in the present simulations. Continued Li incorporation into a-Li$_4$TiS$_4$ would increase the isolated S ions, which may lead to the segregation of Li$_2$S. Figure 6b shows an apparent correlation between the Bader charge and the [33]S nuclear quadrupolar coupling constant (NQCC, $|C_Q|$) calculated for the model structures. The NQCC is defined as follows: $C_Q = eQ\ V_{zz}\ h^{-1}$, where e is the electric charge, Q is the quadrupole moment of the [33]S nucleus, V_{zz} is the largest component of the electric field gradient tensor ($|V_{zz}| \geq |V_{yy}| \geq |V_{xx}|$), and h is Planck's constant. The $S^{\delta-}$ and S^- species showed large C_Q values, indicating that the sulfur species in the disulfide units and polysulfide chains are subject to large electric field gradients, owing to their highly directional covalent S-S bonds.[42] The largest C_Q values of ~45 MHz were obtained for the most oxidized $S^{\delta-}$ ions and were close to that of elemental sulfur.[43] The C_Q values for the relatively ionic S^{2-} species were almost within 10 MHz.[42, 44] These

results indicate that the ^{33}S NQCC is highly sensitive to the valence state of S ions. The calculated ^{33}S isotropic chemical shift (δ_{iso}) is also correlated with the Bader charge for the S^{2-} ions (Figure S11). Although the ^{33}S NMR parameters of the a-TiS$_4$ electrode samples were not obtained because of the difficulty in ^{33}S signal detection due to the limited sample volumes in this study, these results can facilitate the estimation of the valence states of sulfide materials in future studies.

Finally, we briefly discuss the expected conversion process from a-Li$_4$TiS$_4$ to metallic Ti and Li$_2$S. The operando ^{7}Li NMR spectra during the initial discharging down to 0.3 V are shown in Figure 7a (See also Figure S12 for the Li$_x$TiS$_4$ compositions). The discharging profile indicated the extra capacities below 1.75 V, and the final capacity of 1105 mAh g^{-1} was obtained at 0.3 V, which was slightly lower than the theoretical capacity of the proposed reaction: TiS$_4$ + 8Li$^+$ + 8e^- $\rightleftarrows$ Ti + 4Li$_2$S (1217 mAh g^{-1}). Spectral width drastically increased, and the peak position shifted to a higher frequency below 1.75 V. These behaviors suggest increasing dipolar and Fermi contact interactions between the ^{7}Li nuclear spin and the unpaired electrons on the Ti ions. These changes correspond to the appearance of paramagnetic Ti ions in a-Li$_{4+d}$TiS$_4$ ($0 < d < 4$). Therefore, charge compensation is achieved by the reduction of Ti valence below 1.75 V, and the paramagnetic Ti^{3+} (3d^1 electronic configuration) and Ti^{2+} (3d^2) ions become dominant in a-Li$_{3+d}$TiS$_4$. The highest frequency of ~13 ppm was obtained at the Li$_6$TiS$_4$ composition. By further Li insertion, the a-Li$_x$TiS$_4$ signal slightly shifted back to a lower frequency. The estimated composition was Li$_{7.3}$TiS$_4$ at 0.3 V, neglecting the possible contributions from the side reactions. The ^{7}Li MAS NMR spectrum of the sample disassembled at 0.3 V showed two signals (Figure 7b). The sharp signal at 2.8 ppm was assigned to Li$_2$S, whereas the relatively broad signal at ~7 ppm was tentatively attributed to an intermediate phase containing paramagnetic Ti ions (i.e., a-Li$_{4+d}$TiS$_4$, $2 \leq d < 4$). The intensity ratios of the two components were estimated to be 41% and 55%, respectively.

Therefore, the structure of a-$Li_{4+d}TiS_4$ becomes unstable by further Li insertion, and it is expected to decompose into Li_2S. Figure 8 shows the XPS spectra of the sample. The titanium oxide signal at ~458 eV in the Ti 2p core-level spectrum was observed (Figure 8a). A shoulder component at lower binding energies (454–456 eV) should involve contributions from the metallic Ti (453.7 eV[45]) and other reduced titanium sulfides. It is speculated that the particle surface of metallic Ti formed by the conversion reaction is easily oxidized by oxygen from the electrolyte solution. Figure 8b shows the S 2p spectrum, where ~80% of the total intensity was assigned to a highly ionic S^{2-} species (160.4 eV), moderately close to that of Li_2S (160.0 eV). These results demonstrate that the conversion to metallic Ti and Li_2S occurs by further Li insertion into a-Li_4TiS_4 via the formation of a-$Li_{4+d}TiS_4$. Similar conversion process via amorphous Li_xMS_4 has recently been reported for a-VS_4.[46]

4. CONCLUSIONS

Amorphous titanium polysulfide, a-TiS_4, was prepared mechanochemically, and its structural changes during the lithiation/delithiation process were examined in detail using experimental and theoretical techniques. It was found that a-TiS_4 consists of a variety of sulfur chemical states such as S^{2-}, S^-, and $S^{\delta-}$ ($\delta \approx 0$), and the latter two species correspond to the $[S_2]^{2-}$ disulfide unit and/or terminal S, and central S in the -S-S-S- polysulfide chain, respectively. The local structure of a-TiS_4 gradually changed when Li ions were inserted; the disulfide units and polysulfide chains were broken, and the Ti coordination number decreased concomitantly. In the Li_4TiS_4 composition, the highly ionic S^{2-} species became the dominant sulfur chemical state. This indicates that sulfur is a redox-active element, and there is no redox contribution from Ti ion in this composition range. Continued Li insertion into a-Li_4TiS_4 led to the formation of a-$Li_{4+d}TiS_4$ with the reduction of Ti

ions. The conversion to metallic Ti and Li_2S was inferred at 0.3 V. This study demonstrates that structural changes in the amorphous TM polysulfides during Li insertion/extraction are continuous for the bonding nature of sulfide species and the concomitant change in the coordination number of TM ions. The amorphous host structure can accommodate such continuous modifications, which behavior is not topotactic as in conventional crystalline electrode materials. Considering charge compensation mechanism, the anion redox process is reversible in amorphous TM polysulfide electrodes, which is a key factor for stable high-capacity batteries.

Supporting Information

ED pattern, HAADF/BF and EELS STEM images, Raman spectra, and operando ^{7}Li NMR spectra for the a-TiS$_4$ samples, X-ray PDFs, DOS spectra, and ^{33}S NMR shifts calculated for the DFT-MD simulated a-Li$_x$TiS$_4$ (x = 0, 2, and 4) are summarized in the Supporting Information. This information is available free of charge via the Internet at http://pubs.acs.org.

Author Contributions

The manuscript was written through contributions of all authors. All authors have given approval to the final version of the manuscript.

Notes

There are no conflicts to declare.

REFERENCES

1.	Ji, X.; Nazar, L. F. Advances in Li–S Batteries. *J. Mater. Chem.* **2010,** *20*, 9821-9826.

2.	Rauh, R. D.; Shuker, F. S.; Marston, J. M.; Brummer, S. B. Formation of Lithium Polysulfides in Aprotic Media. *J. Inorg. Nucl. Chem.* **1977,** *39*, 1761-1766.

3.	Liu, Q.; Mu, D.; Wu, B.; Wang, L.; Gai, L.; Wu, F. Insight on Lithium Polysulfide Intermediates in a Li/S Battery by Density Functional Theory. *RSC Adv.* **2017,** *7*, 33373-33377.

4.	Ji, X.; Lee, K. T.; Nazar, L. F. A Highly Ordered Nanostructured Carbon-Sulphur Cathode for Lithium-Sulphur Batteries. *Nat. Mater.* **2009,** *8*, 500-506.

5.	Liang, C.; Dudney, N. J.; Howe, J. Y. Hierarchically Structured Sulfur/Carbon Nanocomposite Material for High-Energy Lithium Battery. *Chem. Mater.* **2009,** *21*, 4724-4730.

6.	Zheng, G.; Zhang, Q.; Cha, J. J.; Yang, Y.; Li, W.; Seh, Z. W.; Cui, Y. Amphiphilic Surface Modification of Hollow Carbon Nanofibers for Improved Cycle Life of Lithium Sulfur Batteries. *Nano Lett.* **2013,** *13*, 1265-1270.

7.	Doan-Nguyen, V. V. T.; Subrahmanyam, K. S.; Butala, M. M.; Gerbec, J. A.; Islam, S. M.; Kanipe, K. N.; Wilson, C. E.; Balasubramanian, M.; Wiaderek, K. M.; Borkiewicz, O. J.; Chapman, K. W.; Chupas, P. J.; Moskovits, M.; Dunn, B. S.; Kanatzidis, M. G.; Seshadri, R. Molybdenum Polysulfide Chalcogels as High-Capacity, Anion-Redox-Driven Electrode Materials for Li-Ion Batteries. *Chem. Mater.* **2016,** *28*, 8357-8365.

8.	Wang, X.; Du, K.; Wang, C.; Ma, L.; Zhao, B.; Yang, J.; Li, M.; Zhang, X. X.; Xue, M.; Chen, J. Unique Reversible Conversion-Type Mechanism Enhanced Cathode Performance in Amorphous Molybdenum Polysulfide. *ACS Appl. Mater. Interfaces* **2017,** *9*, 38606-38611.

9.	Sakuda, A.; Taguchi, N.; Takeuchi, T.; Kobayashi, H.; Sakaebe, H.; Tatsumi, K.; Ogumi, Z. Amorphous TiS_4 Positive Electrode for Lithium–Sulfur Secondary Batteries. *Electrochem. Commun.* **2013,** *31*, 71-75.

10.   Sakuda, A.; Taguchi, N.; Takeuchi, T.; Kobayashi, H.; Sakaebe, H.; Tatsumi, K.; Ogumi, Z. Composite Positive Electrode Based on Amorphous Titanium Polysulfide for Application in All-Solid-State Lithium Secondary Batteries. *Solid State Ion.* **2014,** *262*, 143-146.

11.   Sakuda, A.; Taguchi, N.; Takeuchi, T.; Kobayashi, H.; Sakaebe, H.; Tatsumi, K.; Ogumi, Z. Amorphous Niobium Sulfides as Novel Positive-Electrode Materials. *ECS Electrochem. Lett.* **2014,** *3*, A79-A81.

12.   Sakuda, A.; Takeuchi, T.; Okamura, K.; Kobayashi, H.; Sakaebe, H.; Tatsumi, K.; Ogumi, Z. Rock-Salt-Type Lithium Metal Sulphides as Novel Positive-Electrode Materials. *Sci. Rep.* **2014,** *4*, 4883.

13.   Matsuyama, T.; Hayashi, A.; Ozaki, T.; Mori, S.; Tatsumisago, M. Electrochemical Properties of All-Solid-State Lithium Batteries with Amorphous MoS_3 Electrodes Prepared by Mechanical Milling. *J. Mater. Chem. A* **2015,** *3*, 14142-14147.

14.   Sakuda, A.; Takeuchi, T.; Shikano, M.; Ohara, K.; Fukuda, K.; Uchimoto, Y.; Ogumi, Z.; Kobayashi, H.; Sakaebe, H. Development of Li_2TiS_3-Li_3NbS_4 by a Mechanochemical Process. *J. Ceram. Soc. Jpn* **2017,** *125*, 268-271.

15.   Takeuchi, T.; Kageyama, H.; Nakanishi, K.; Ogawa, M.; Ohta, T.; Sakuda, A.; Sakaebe, H.; Kobayashi, H.; Ogumi, Z. Preparation of Li_2S-FeS_x Composite Positive Electrode Materials and Their Electrochemical Properties with Pre-Cycling Treatments. *J. Electrochem. Soc.* **2015,** *162*, A1745-A1750.

16.   Shimoda, K.; Murakami, M.; Takeuchi, T.; Matsunaga, T.; Ukyo, Y.; Sakaebe, H.; Kobayashi, H.; Matsubara, E. Structural and Dynamic Behavior of Lithium Iron Polysulfide Li_8FeS_5 During Charge–Discharge Cycling. *J. Power Sources* **2018,** *398*, 67-74.

17.   Allman, R.; Baumann, I.; Kutoglu, A.; Rosch, H.; Hellner, E. Die Kristallstruktur des Patronits $V(S_2)_2$. *Sci. Nat.* **1964,** *51*, 263-264.

18. Kozlova, M. N.; Mironov, Y. V.; Grayfer, E. D.; Smolentsev, A. I.; Zaikovskii, V. I.; Nebogatikova, N. A.; Podlipskaya, T. Y.; Fedorov, V. E. Synthesis, Crystal Structure, and Colloidal Dispersions of Vanadium Tetrasulfide (VS_4). *Chem. Eur. J.* **2015,** *21*, 4639-4645.

19. Rout, C. S.; Kim, B. H.; Xu, X.; Yang, J.; Jeong, H. Y.; Odkhuu, D.; Park, N.; Cho, J.; Shin, H. S. Synthesis and Characterization of Patronite Form of Vanadium Sulfide on Graphitic Layer. *J. Am. Chem. Soc.* **2013,** *135*, 8720-8725.

20. Britto, S.; Leskes, M.; Hua, X.; Hebert, C. A.; Shin, H. S.; Clarke, S.; Borkiewicz, O.; Chapman, K. W.; Seshadri, R.; Cho, J.; Grey, C. P. Multiple Redox Modes in the Reversible Lithiation of High-Capacity, Peierls-Distorted Vanadium Sulfide. *J. Am. Chem. Soc.* **2015,** *137*, 8499-8508.

21. Koganei, K.; Sakuda, A.; Takeuchi, T.; Kiuchi, H.; Sakaebe, H. Improvement of Electrochemical Property of VS_4 Electrode Material by Amorphization via Mechanical Milling Process. *Electrochemistry* **2021,** *89*, 239-243.

22. Shimoda, K.; Koganei, K.; Takeuchi, T.; Matsunaga, T.; Murakami, M.; Sakaebe, H.; Kobayashi, H.; Matsubara, E. Structural Characterization of an Amorphous VS_4 and Its Lithiation/Delithiation Behavior Studied by Solid-State NMR Spectroscopy. *RSC Adv.* **2019,** *9*, 23979-23985.

23. Sakuda, A.; Ohara, K.; Fukuda, K.; Nakanishi, K.; Kawaguchi, T.; Arai, H.; Uchimoto, Y.; Ohta, T.; Matsubara, E.; Ogumi, Z.; Okumura, T.; Kobayashi, H.; Kageyama, H.; Shikano, M.; Sakaebe, H.; Takeuchi, T. Amorphous Metal Polysulfides: Electrode Materials with Unique Insertion/Extraction Reactions. *J. Am. Chem. Soc.* **2017,** *139*, 8796-8799.

24. Grayfer, E. D.; Pazhetnov, E. M.; Kozlova, M. N.; Artemkina, S. B.; Fedorov, V. E. Anionic Redox Chemistry in Polysulfide Electrode Materials for Rechargeable Batteries. *ChemSusChem* **2017,** *10*, 4805-4811.

25.   Saha, S.; Assat, G.; Sougrati, M. T.; Foix, D.; Li, H.; Vergnet, J.; Turi, S.; Ha, Y.; Yang, W.; Cabana, J.; Rousse, G.; Abakumov, A. M.; Tarascon, J.-M. Exploring the Bottlenecks of Anionic Redox in Li-Rich Layered Sulfides. *Nat. Energy* **2019,** *4*, 977-987.

26.   Flamary-Mespoulie, F.; Boulineau, A.; Martinez, H.; Suchomel, M. R.; Delmas, C.; Pecquenard, B.; Le Cras, F. Lithium-Rich Layered Titanium Sulfides: Cobalt- and Nickel-Free High Capacity Cathode Materials for Lithium-Ion Batteries. *Energy Stor. Mater.* **2020,** *26*, 213-222.

27.   Shimoda, K.; Murakami, M.; Takamatsu, D.; Arai, H.; Uchimoto, Y.; Ogumi, Z. In Situ NMR Observation of the Lithium Extraction/Insertion from $LiCoO_2$ Cathode. *Electrochim. Acta* **2013,** *108*, 343-349.

28.   Clark, S. J.; Segall, M. D.; Picard, C. J.; Hasnip, P. J.; Probert, M. I. J.; Refson, K.; Payne, M. C. First Principles Methods Using CASTEP. *Z. Kristallogr.* **2005,** *220*, 567-570.

29.   Perdew, J. P.; Ruzsinszky, A.; Csonka, G. I.; Vydrov, O. A.; Scuseria, G. E.; Constantin, L. A.; Zhou, X.; Burke, K. Restoring the Density-Gradient Expansion for Exchange in Solids and Surfaces. *Phys. Rev. Lett.* **2008,** *100*, 136406.

30.   Krukau, A. V.; Vydrov, O. A.; Izmaylov, A. F.; Scuseria, G. E. Influence of the Exchange Screening Parameter on the Performance of Screened Hybrid Functionals. *J. Chem. Phys.* **2006,** *125*, 224106.

31.   Pickard, C. J.; Mauri, F. All-Electron Magnetic Response with Pseudopotentials: NMR Chemical Shifts. *Phys. Rev. B* **2001,** *63*, 245101.

32.   Yates, J. R.; Pickard, C. J.; Mauri, F. Calculation of NMR Chemical Shifts for Extended Systems Using Ultrasoft Pseudopotentials. *Phys. Rev. B* **2007,** *76*, 024401.

33.   Momma, K.; Izumi, F. VESTA 3 for Three-Dimensional Visualization of Crystal, Volumetric and Morphology Data. *J. Appl. Crystallogr.* **2011,** *44*, 1272-1276.

34.   Pawbake, A. S.; Island, J. O.; Flores, E.; Ares, J. R.; Sanchez, C.; Ferrer, I. J.; Jadkar, S. R.; van der Zant, H. S.; Castellanos-Gomez, A.; Late, D. J. Temperature-Dependent Raman Spectroscopy of Titanium Trisulfide (TiS$_3$) Nanoribbons and Nanosheets. *ACS Appl Mater Interfaces* **2015,** *7*, 24185-24190.

35.   Lindic, M. H.; Martinez, H.; Benayad, A.; Pecquenard, B.; Vinatier, P.; Levasseur, A.; Gonbeau, D. XPS Investigations of TiO$_y$S$_z$ Amorphous Thin Films Used as Positive Electrode in Lithium Microbatteries. *Solid State Ion.* **2005,** *176*, 1529-1537.

36.   Fleet, M. E.; Harmer, S. L.; Liu, X.; Nesbitt, H. W. Polarized X-ray Absorption Spectroscopy and XPS of TiS$_3$: S K- and Ti L-edge XANES and S and Ti 2p XPS. *Surf. Sci.* **2005,** *584*, 133-145.

37.   Matsuyama, T.; Deguchi, M.; Mitsuhara, K.; Ohta, T.; Mori, T.; Orikasa, Y.; Uchimoto, Y.; Kowada, Y.; Hayashi, A.; Tatsumisago, M. Structure Analyses Using X-ray Photoelectron Spectroscopy and X-ray Absorption Near Edge Structure for Amorphous MS$_3$ (M: Ti, Mo) Electrodes in All-Solid-State Lithium Batteries. *J.Power Sources* **2016,** *313*, 104-111.

38.   Smart, R. S. C.; Skinner, W. M.; Gerson, A. R. XPS of Sulphide Mineral Surfaces: Metal-deficient, Polysulphides, Defects and Elemental Sulphur. *Surf. Interface Anal.* **1999,** *28*, 101-105.

39.   Demir-Cakan, R.; Morcrette, M.; Nouar, F.; Davoisne, C.; Devic, T.; Gonbeau, D.; Dominko, R.; Serre, C.; Ferey, G.; Tarascon, J.-M. Cathode Composites for Li-S Batteries via the Use of Oxygenated Porous Architectures. *J. Am. Chem. Soc.* **2011,** *133*, 16154-16160.

40.   Bader, R. F. W. Atoms in Molecules. *Acc. Chem. Res.* **1985,** *18*, 9-15.

41.   Henkelman, G.; Arnaldsson, A.; Jónsson, H. A Fast and Robust Algorithm for Bader Decomposition of Charge Density. *Comput. Mater. Sci.* **2006,** *36*, 354-360.

42.   Halat, D. M.; Britto, S.; Griffith, K. J.; Jonsson, E.; Grey, C. P. Natural Abundance Solid-State ^{33}S NMR Study of NbS$_3$: Applications for Battery Conversion Electrodes. *Chem. Commun.* **2019,** *55*, 12687-12690.

43.   O'Dell, L. A.; Moudrakovski, I. L. Testing the Sensitivity Limits of ^{33}S NMR: an Ultra-Wideline Study of Elemental Sulfur. *J. Magn. Reson.* **2010,** *207*, 345-347.

44.   Sutrisno, A.; Terskikh, V. V.; Huang, Y. A Natural Abundance ^{33}S Solid-State NMR Study of Layered Transition Metal Disulfides at Ultrahigh Magnetic Field. *Chem. Commun.* **2009**, 186-188.

45.   Biesinger, M. C.; Lau, L. W. M.; Gerson, A. R.; Smart, R. S. C. Resolving Surface Chemical States in XPS Analysis of First Row Transition Metals, Oxides and Hydroxides: Sc, Ti, V, Cu and Zn. *Appl. Surf. Sci.* **2010,** *257*, 887-898.

46.   Shimoda, K.; Takeuchi, T.; Murakami, M.; Sakaebe, H. Reversible Lithium Insertion and Conversion Process of Amorphous VS$_4$ Revealed by Operando Electrochemical NMR Spectroscopy. *Solid State Ion.* **2022,** *380*, 115920.

Table 1. Average Bader charge and [33]S NQCCs calculated for a-Li$_x$TiS$_4$ (x = 0, 2, and 4) and reference materials.

	Ti / e	S / e	[33]S $|C_Q|$ / MHz
a-TiS$_4$	1.64[a]	–0.41[a]	28.3[a]
a-Li$_2$TiS$_4$	1.67[a]	–0.92[a]	20.0[a]
a-Li$_4$TiS$_4$	1.68[a]	–1.42[a]	4.2[a]
TiS$_2$	1.70	–0.85	1.3
LiTiS$_2$	1.57	–1.28	0.5
TiS$_3$	1.63	–0.38	33.4
		–0.87	2.8
Li$_2$S	-	–2.0	0.0
S (α-S$_8$)	-	0.0[a]	40.2[a]

[a] Average value

Figures and Figure captions
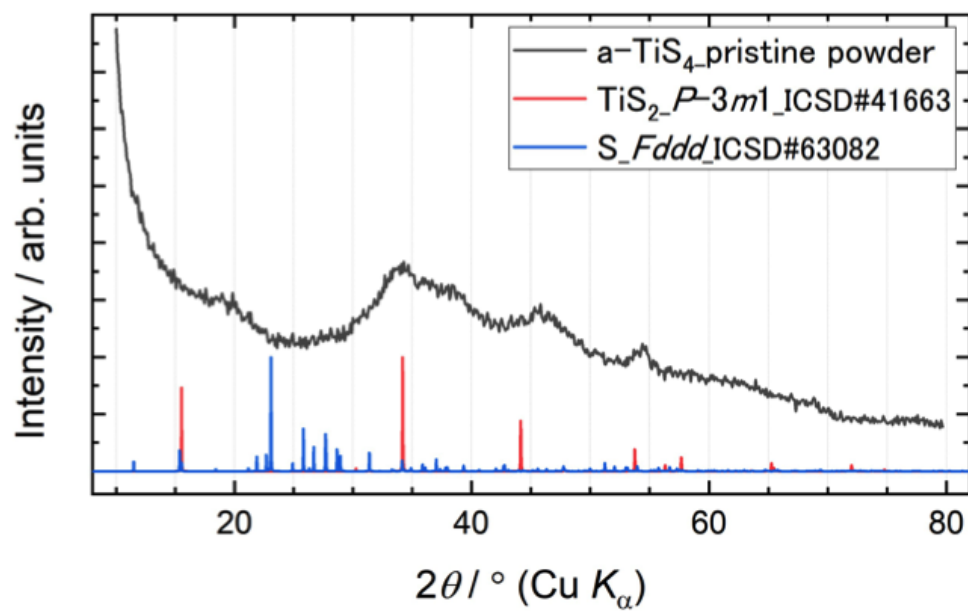
Figure 1.

XRD profile of the mechanochemically synthesized a-TiS₄ powder.
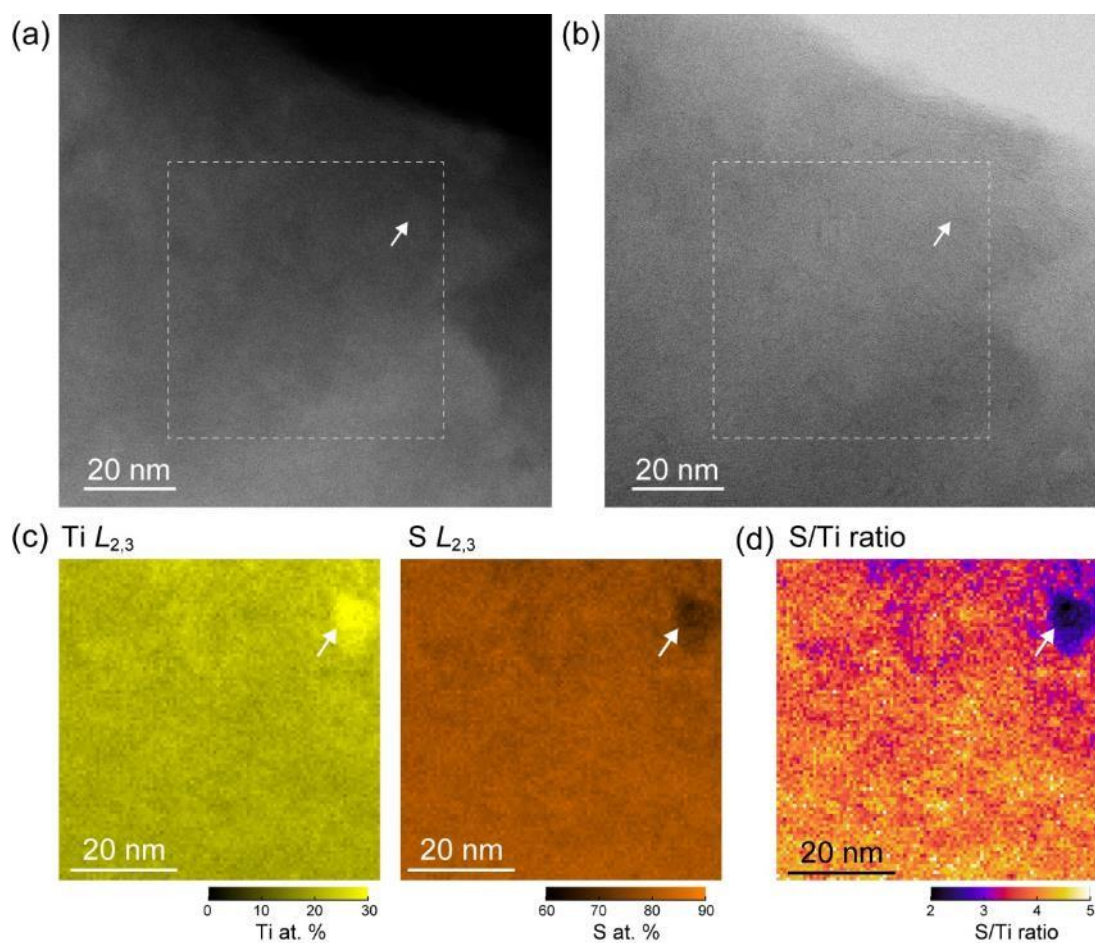
Figure 2.

(a) HAADF and (b) BF STEM images of the pristine a-TiS$_4$ powder. (c) EELS composition maps

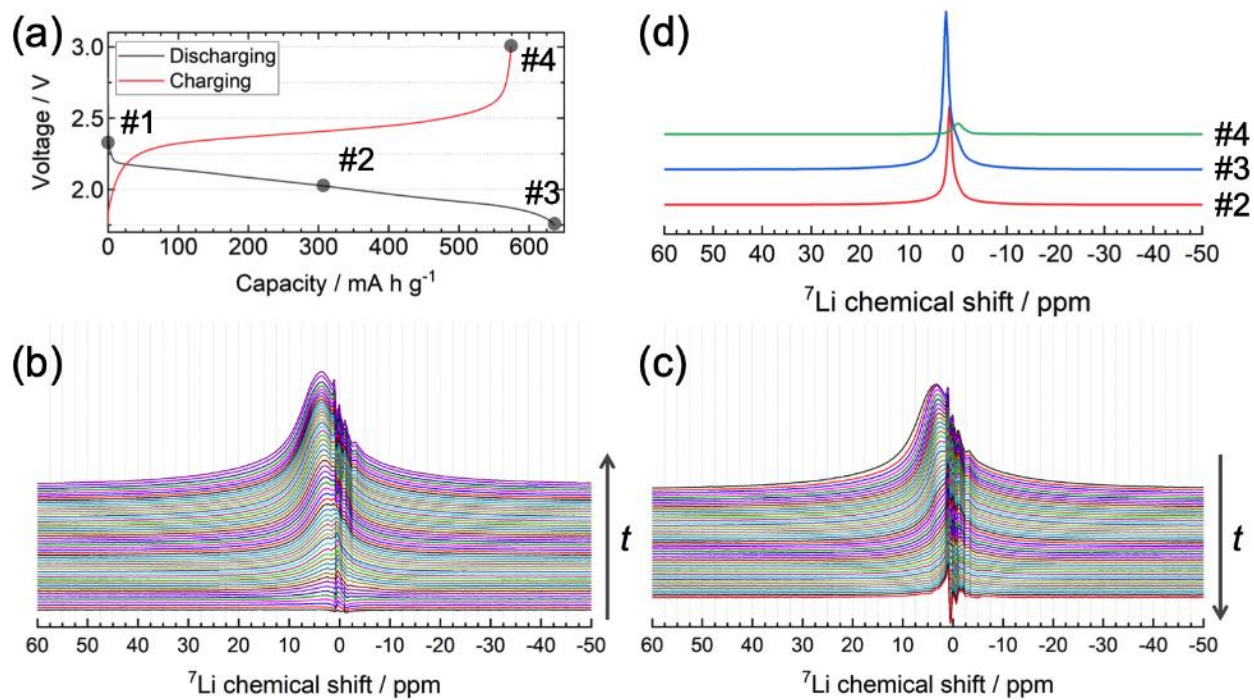of Ti and S and (d) S/Ti ratio map obtained for the square region in (a,b).

Figure 3.

(a) Discharge-charge profile of a-TiS$_4$ in a voltage window between 1.75 and 3.0 V. Time evolution of operando ^{7}Li NMR spectra of the Li//a-TiS$_4$ cell during (b) discharging and (c) charging process. (d) ^{7}Li MAS NMR spectra of the a-TiS$_4$ electrode samples disassembled at the discharged and charged states shown in (a).
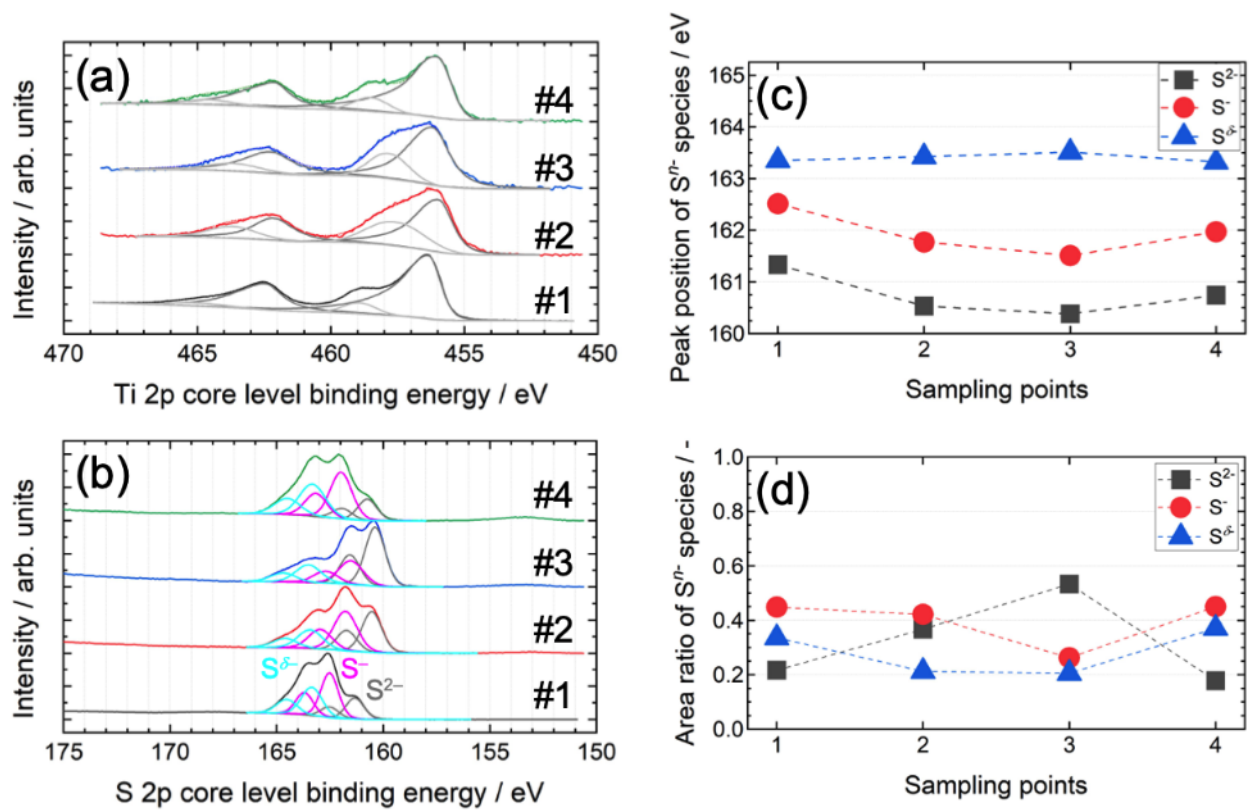
Figure 4.

(a) Ti 2p and (b) S 2p XPS spectra of the a-TiS$_4$ electrode samples. The sample numbers are same as in Figure 3a. (c) Peak position and (d) peak area ratio of the S^{2-}, S$^-$, and S$^{\delta-}$ species extracted from (b).
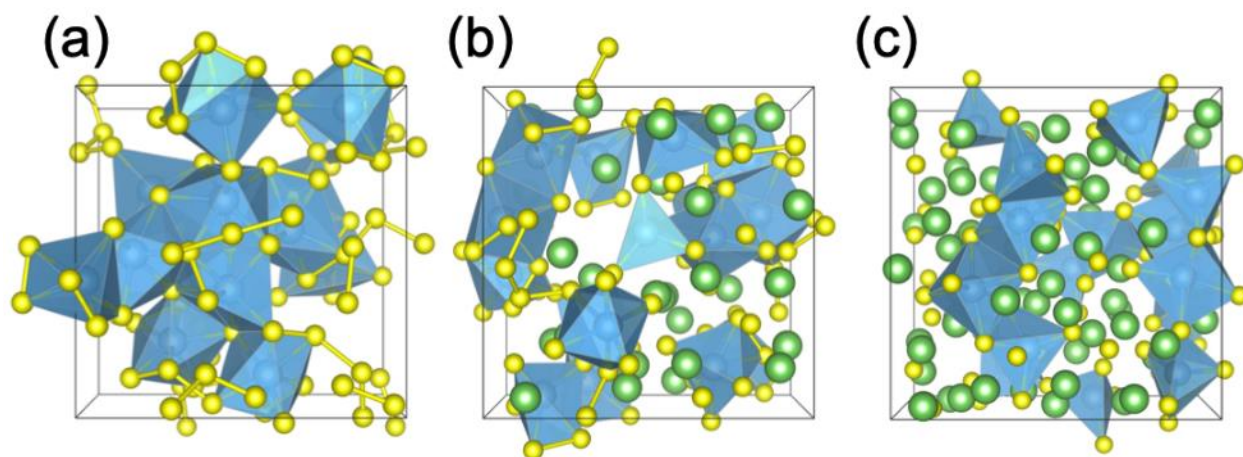
Figure 5.

DFT-MD simulated structures of (a) a-TiS$_4$, (b) a-Li$_2$TiS$_4$, and (c) a-Li$_4$TiS$_4$ (S: yellow ball, Ti: blue polyhedron, Li: green ball). The S-S bonds in disulfide units and polysulfide chains are shown within a cut-off of 2.4 Å.

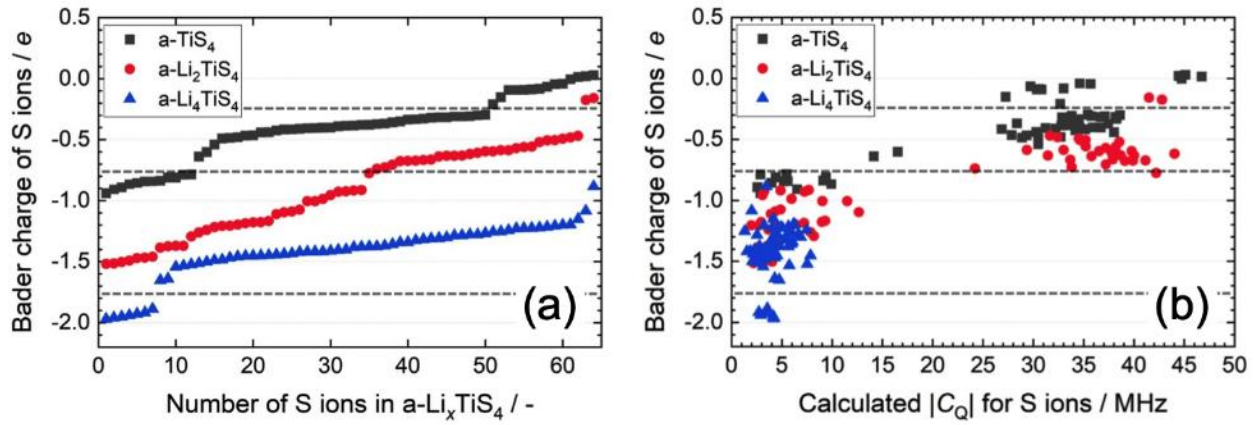**Figure 6.**

(a) Bader charge distribution of S ions for the DFT-MD simulated a-Li$_x$TiS$_4$ (x = 0, 2, and 4). The horizontal axis indicates the number of S ions aligned in order of increasing charge for clarity. (b) Bader charge distribution of S ions as a function of the nuclear quadrupolar coupling constant |C_Q|.
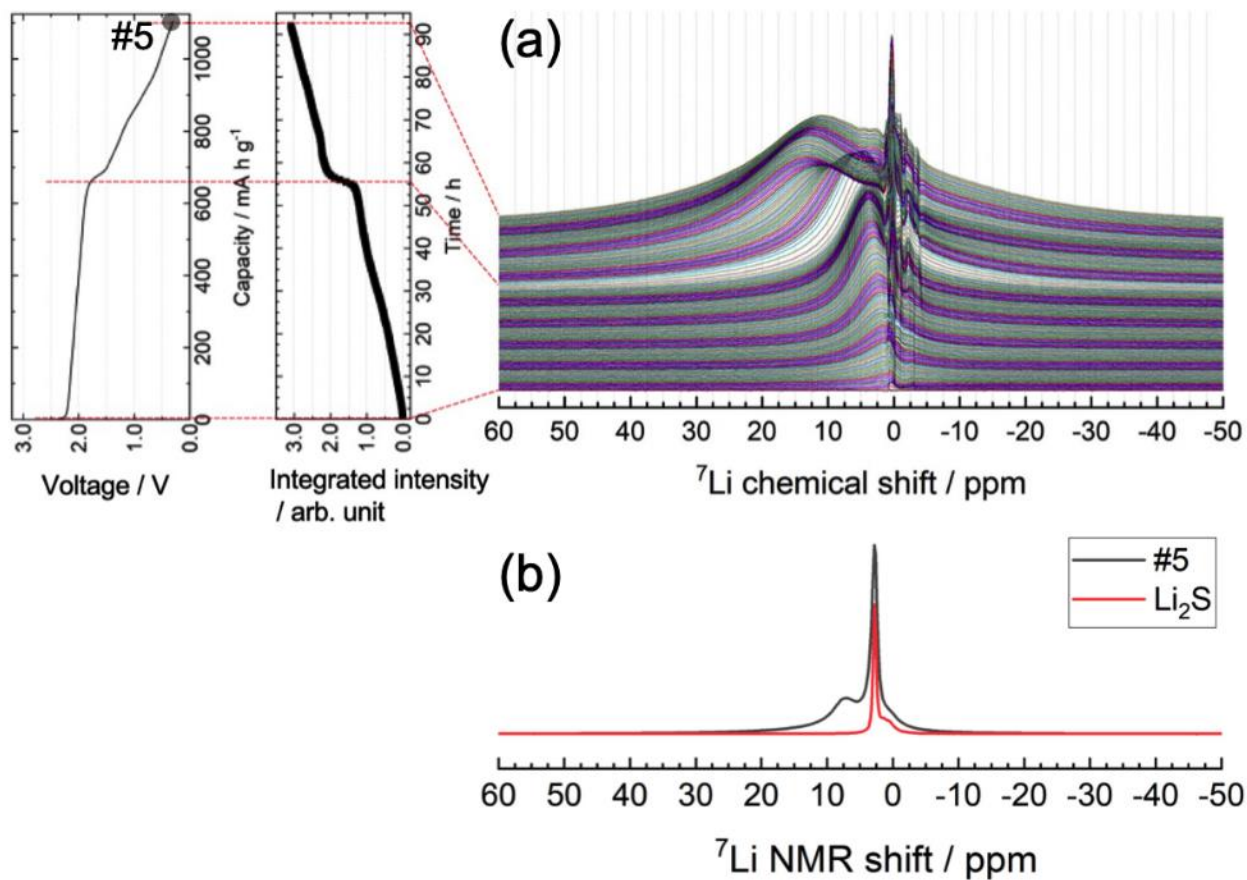
Figure 7.

(a) Time evolution of operando ^{7}Li NMR spectra of the Li//a-TiS$_4$ cell along with the discharging profile down to 0.3 V and the integrated intensity evolution of the a-Li$_x$TiS$_4$ signal (including residual electrolyte signal). The electrochemical measurements were performed at a current density of 12.2 mA g^{-1} (0.01 C rate). (b) ^{7}Li MAS NMR spectrum of the a-TiS$_4$ electrode sample disassembled at 0.3 V (#5) with that of Li$_2$S as a reference.
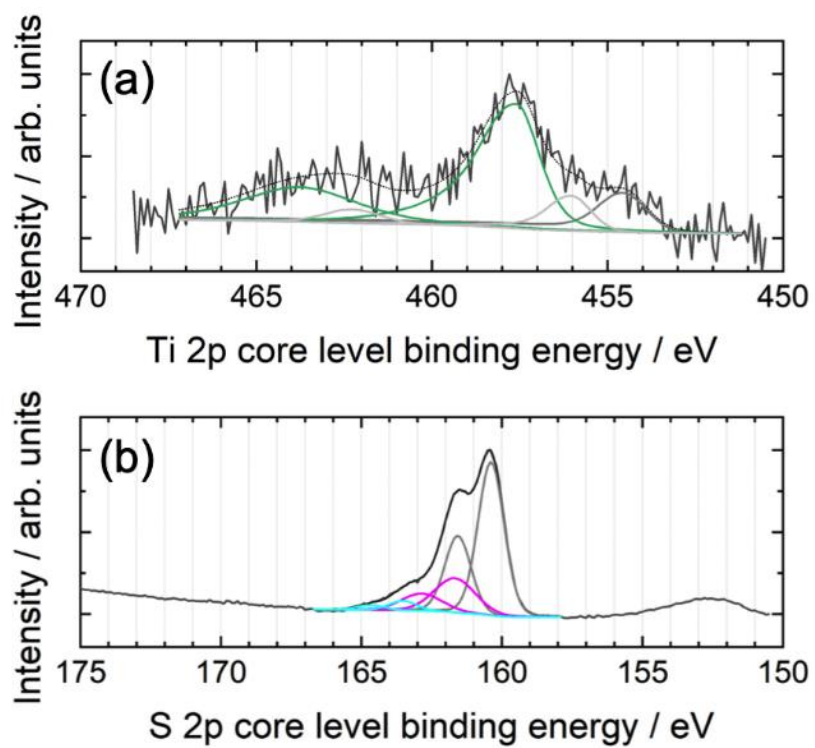
Figure 8.

(a) Ti 2p and (b) S 2p XPS spectra of the a-TiS_4 electrode sample disassembled at 0.3 V (#5).

Table of Contents

TiS$_2$

S

High-energy
Ball milling

a-TiS$_4$

+ Li

− Li

a-Li$_{\sim 4}$TiS$_4$